BIOCHEMISTRY

Multiple modes of PRC2 inhibition elicit global chromatin alterations in H3K27M pediatric glioma

James M. Stafford[1,2]*, Chul-Hwan Lee[1,2]*, Philipp Voigt[1†], Nicolas Descostes[1,2], Ricardo Saldaña-Meyer[1,2], Jia-Ray Yu[1,2], Gary Leroy[1,2], Ozgur Oksuz[1,2], Jessica R. Chapman[3‡], Fernando Suarez[4,5], Aram S. Modrek[4,6], N. Sumru Bayin[4,6], Dimitris G. Placantonakis[4,6,7,8], Matthias A. Karajannis[4,5§], Matija Snuderl[4,9], Beatrix Ueberheide[1,3], Danny Reinberg[1,2‖]

A methionine substitution at lysine-27 on histone H3 variants (H3K27M) characterizes ~80% of diffuse intrinsic pontine gliomas (DIPG) and inhibits polycomb repressive complex 2 (PRC2) in a dominant-negative fashion. Yet, the mechanisms for this inhibition and abnormal epigenomic landscape have not been resolved. Using quantitative proteomics, we discovered that robust PRC2 inhibition requires levels of H3K27M greatly exceeding those of PRC2, seen in DIPG. While PRC2 inhibition requires interaction with H3K27M, we found that this interaction on chromatin is transient, with PRC2 largely being released from H3K27M. Unexpectedly, inhibition persisted even after PRC2 dissociated from H3K27M-containing chromatin, suggesting a lasting impact on PRC2. Furthermore, allosterically activated PRC2 is particularly sensitive to H3K27M, leading to the failure to spread H3K27me from PRC2 recruitment sites and consequently abrogating PRC2's ability to establish H3K27me2-3 repressive chromatin domains. In turn, levels of polycomb antagonists such as H3K36me2 are elevated, suggesting a more global, downstream effect on the epigenome. Together, these findings reveal the conditions required for H3K27M-mediated PRC2 inhibition and reconcile seemingly paradoxical effects of H3K27M on PRC2 recruitment and activity.

INTRODUCTION

Histones form the core DNA packaging material in the nucleus. Even slight alterations in their amino acid composition can have dramatic consequences on chromatin structure, affecting gene expression and genome integrity (*1*). One of the most marked examples is the lysine-to-methionine (K-to-M) substitution at residue 27 on canonical histone H3.1 or its variant H3.3 (H3K27M). These mutations were found in ~80% of diffuse intrinsic pontine gliomas (DIPG), one of the most deadly and difficult-to-treat pediatric cancers (*2*). Despite affecting only 1 of 15 copies of the H3 genes, the presence of H3K27M significantly impairs the activity of polycomb repressive complex 2 (PRC2), leading to a drastic reduction and redistribution of di- and trimethylation of H3K27 (H3K27me2 and H3K27me3, respectively) (*3*–*6*) in the affected cells. These effects of H3K27M on PRC2, as well as those on the chromatin landscape, have been linked to oncogenic transcriptional programs that give rise to the cancer stem cell–like and proliferative properties of DIPG (*4*, *7*, *8*). Therefore, understanding the underlying mechanisms of how H3K27M affects PRC2 and the global epigenetic landscape is imperative for understanding DIPG, and ultimately, devising strategic ways to overcome the oncogenic potential of H3K27M.

[1]Department of Biochemistry and Molecular Pharmacology, NYUSoM, New York, NY, USA. [2]Howard Hughes Medical Institute, Chevy Chase, MD, USA. [3]Proteomics Laboratory, NYUSoM, New York, NY, USA. [4]Laura and Isaac Perlmutter Cancer Center, NYUSoM, New York, NY, USA. [5]Department of Pediatrics, NYUSoM, New York, NY, USA. [6]Department of Neurosurgery, NYUSoM, New York, NY, USA. [7]Kimmel Center for Stem Cell Biology, NYUSoM, New York, NY, USA. [8]Neuroscience Institute, NYUSoM, New York, NY, USA. [9]Department of Pathology, Division of Neuropathology, NYUSoM, New York, NY, USA.
*These authors contributed equally to this work.
†Present address: Wellcome Centre for Cell Biology, School of Biological Sciences, University of Edinburgh, Edinburgh, UK.
‡Present address: Department of Pathology, Memorial Sloan Kettering Cancer Center, New York, NY, USA.
§Present address: Department of Pediatrics, Memorial Sloan Kettering Cancer Center, New York, NY, USA.
‖Corresponding author. Email: danny.reinberg@nyumc.org

Following the discovery of H3K27M, a hypothesis suggesting that H3K27M traps and sequesters PRC2, thereby diminishing its activity, emerged (*3*). Supporting evidence came from the observation that PRC2 has a higher affinity for H3K27M relative to WT H3K27 (H3K27WT) peptides and nucleosomes (*4*, *9*). Moreover, structural studies revealed that H3K27M occupies the catalytic su(var)3-9, enhancer-of-zeste and trithorax (SET) domain of enhancer-of-zeste homolog 2 (EZH2), preventing the hydrolysis of the methyl donor *S*-adenosylmethionine (SAM) and the release of EZH2 (*3*, *4*, *9*). However, in vivo studies indicate that the genomic localization of H3K27M is often inversely correlated with PRC2 occupancy, challenging the idea that H3K27M sequesters PRC2 on chromatin (*6*, *10*, *11*). Notably, despite a drastic loss in H3K27me3 in affected cells, some loci retained PRC2 and H3K27me3 at abnormally high levels in H3K27M-expressing cells (*4*, *5*, *12*). Additional layers of complexity came from studies showing that H3K27M does not have consistent effects in all cell types (*7*, *8*) nor is it able to strongly interact with PRC2 in all chromatin contexts (*6*, *13*). Therefore, a model whereby H3K27M stably sequesters PRC2 on chromatin cannot explain all observations, indicating that further study is required to resolve these disparate observations and to uncover the mechanism(s) by which H3K27M affects PRC2 and the chromatin landscape in DIPG. This study aims to reconcile these findings by combining isogenic and patient-derived model systems to better understand the dynamic and nuanced impact of H3K27M on PRC2 while placing those effects in the molecular and broader chromatin context.

RESULTS

H3K27M-to-PRC2 ratio dictates the degree of PRC2 inhibition

Perhaps the most studied hypothesis for dominant-negative inhibition of PRC2 by H3K27M is that H3K27M sequesters PRC2, preventing it from methylating most of H3K27WT nucleosomes (*3*, *4*, *9*, *14*). This hypothesis relies on two assumptions, namely, that H3K27M is

more abundant than PRC2 and that PRC2 has a higher affinity for H3K27M- than H3K27WT-containing nucleosomes. Therefore, precise quantification of PRC2 relative to H3K27 methylation (H3K27me) and H3K27M levels in DIPGs and comparable cell types is essential for understanding how the cellular stoichiometry of these factors contributes to cellular sensitivity to H3K27M. We hypothesized that the levels of PRC2 might render DIPG particularly sensitive to H3K27M, given their profound loss in H3K27me2-3 relative to other brain tumors and cell types in the neural lineage (Fig. 1A).

Testing this hypothesis required a quantitative measure of PRC2 molecules per cell, leading us to develop an MS parallel reaction monitoring assay (*15*). Briefly, PRC2 core proteins [EZH2, embryonic ectoderm development (EED), and suppressor of zeste homolog 12 (SUZ12)] were quantified with a targeted method using heavy isotope-labeled synthetic peptides as internal standards (fig. S1, A to C, and data file S1). Our approach revealed a wide range of PRC2 levels across different cell types, with CRISPR-generated H3K27M (on H3F3A) E14 mESCs containing relatively high PRC2 levels (~150,000 PRC2 molecules per cell; Fig. 1B and fig. S1D). In our isogenic mESC and 293 T-REx system below, we chose H3.3K27M, as it is the most frequently occurring H3K27M mutation (*2*). H3K27M DIPGs (both H3.1K27M and H3.3K27M DIPGs) were at the lower end of the spectrum (~5 to 10,000 PRC2 molecules per cell; fig. S1D). By comparing the levels of PRC2 with those of H3K27M, as determined by relative quantitative histone MS, we observed that H3K27M-bearing DIPG exhibited ~100-fold excess of H3K27M over PRC2 (Fig. 1B and see table S1 for details on cell lines). In accordance, H3K27M-bearing DIPGs showed a robust loss in H3K27me2-3 deposition relative to WT DIPG (Fig. 1B). Similarly, 293 T-REx cells with inducible expression of H3K27M (H3.3K27M) also showed a large excess of H3K27M relative to PRC2 (more than 200-fold) and a substantial deficit in H3K27me2-3. However, mESC harboring H3.3K27M showed only a modest loss in H3K27me2-3, relative to WT mESC. Given that H3K27M was only in ~10-fold excess of PRC2 in mESC, the results suggested that H3K27M must be largely in excess of PRC2 to achieve the robust decrease in H3K27me2-3 seen in DIPG and other cell types. These results are consistent with previous speculation that high amounts of a K-to-M mutation are needed to inhibit various HMTs (*3*, *16*).

To test whether shifting the relative abundance of H3K27M and PRC2 during lineage commitment could alter sensitivity to H3K27M inhibition, we differentiated H3.3K27M mESC as described above into cervical mNEURON precursors (Fig. 1C) (*17*). Our quantitative MS revealed that PRC2 decreased as cells proceeded down the mNEURON lineage to levels consistent with those seen in DIPG (5 to 10,000 molecules per cell; fig S1). We observed that K27M produced a greater loss of H3K27me2-3 in mNEURON than was seen in undifferentiated mESC (Fig. 1D). Although we cannot rule out the contribution of an unknown factor(s) during the differentiation process, these results, together with those analyzing the quantitative H3K27M-to-PRC2 ratio in different cells, demonstrate that the critical force for the H3K27me3 reduction is due to the large excess of K27M over PRC2. These observations are consistent with K27me2-3 loss when the H3K27M-to-PRC2 ratio is high, which we tested directly using an HMT assay in a fully biochemically reconstituted system (Fig. 1E). The addition of increasing amounts of recombinant oligonucleosomes comprising H3K27M gave rise to heightened sensitivity of PRC2 to inhibition, while the control using oligonucleosomes where lysine-27 was mutated to alanine (H3K27A) was ineffectual (Fig. 1E). Together, the quantitative approach measuring H3K27M-to-PRC2 ratio in different cell lines including patient-derived DIPG model systems, as well as the in vitro differentiation studies together with the biochemical approach, revealed that cells containing low amounts of PRC2, relative to H3K27M such as DIPG, mNEURONs, and 293 T-REx, are sensitive to H3K27M-mediated inhibition of PRC2 activity.

PRC2 is transiently recruited to H3K27M-containing chromatin

Given the high excess of H3K27M to PRC2 in DIPG (Fig. 1B) and the higher affinity of PRC2 for H3K27M in vitro, H3K27M would be expected to sequester all PRC2 in a DIPG cell (*3*, *9*, *16*). However, the following observations argue against this assumption: (i) PRC2 and H3K27M often do not colocalize on chromatin under some conditions of steady-state H3K27M expression, as measured by chromatin immunoprecipitation (ChIP) (*6*, *10*, *18*); and (ii) H3K27me3 can be retained at specific loci and redistributed in H3K27M cells (*4*–*6*, *10*, *12*). Reasoning that the steady-state dynamics between H3K27M and PRC2 reflect only the outcome of this dysregulated process, we sought a means to detect changes in the interaction between H3K27me3 and PRC2 and subsequent effects on PRC2 as a function of the rate of H3K27M deposition. To this end, we used an inducible expression system in 293 T-REx cells to monitor the early and later events following H3K27M expression (Fig. 2A). This inducible system recapitulated the global loss of H3K27me2-3 seen in H3K27M-bearing DIPG (Figs. 2B and 1A). Spike-in normalized ChIP sequencing (ChIP-seq) experiments across this time course revealed that PRC2 primarily colocalized with H3K27M at early time points, namely, after 6 and 12 hours of expression, but was largely excluded from H3K27M sites at the late, 24-hour time point (Fig. 2C, left). Genome-wide analysis indicated that there are nearly 1500 PRC2-occupied domains unique to the 6- and 12-hour time points that are not present at 24 hours (Fig. 2C, right). Those early PRC2 loci are only seen in H3K27M-, but not in H3K27WT-expressing, cells and colocalized with H3K27M (Fig. 2C). Combined with the higher affinity of PRC2 for H3K27M nucleosomes [(*4*) and see below] and peptides (*9*), our results demonstrate that H3K27M-containing nucleosomes transiently recruit PRC2 to loci not typically occupied by PRC2 in a WT setting, leading to the aberrant deposition of PRC2 early after H3K27M expression (Fig. 2).

Given the transient nature of PRC2 recruitment to H3K27M, numerous factors might contribute to its eviction, including the known PRC2 antagonist, H3K36me2, especially when it occurs directly adjacent to H3K27M (i.e., in cis). Western blot analysis of extracts derived from the inducible 293 T-REx system revealed enrichment of H3K36me2 on H3.3K27M histones, supporting their co-occurrence in cis, which coincided with a loss of H3K27me2-3 (Fig. 2B). This was particularly evident in H3K27M-bearing DIPG, where MS revealed that H3K36me2 was overwhelmingly the predominant modification adjacent to H3K27M, regardless of whether it was H3.1K27M or H3.3K27M (fig. S2A). In our time course studies, a strong co-occurrence in cis of H3K36me2 and H3K27M emerged at 24 hours, at which time EZH2 occupancy at H3K27M-containing loci is lost, relative to earlier time points (Fig. 2B). Therefore, eventual PRC2 eviction and stable exclusion from K27M loci might be related to H3K36me2 deposition, presumably by preventing PRC2 interaction with the H3 N-terminal tail (*19*–*22*). Other antagonistic modifications such as histone acetylation might also contribute, as has been suggested by others [(*6*, *13*) and see our data below]. In a broad sense, the deposition of H3K27M largely into transcriptionally

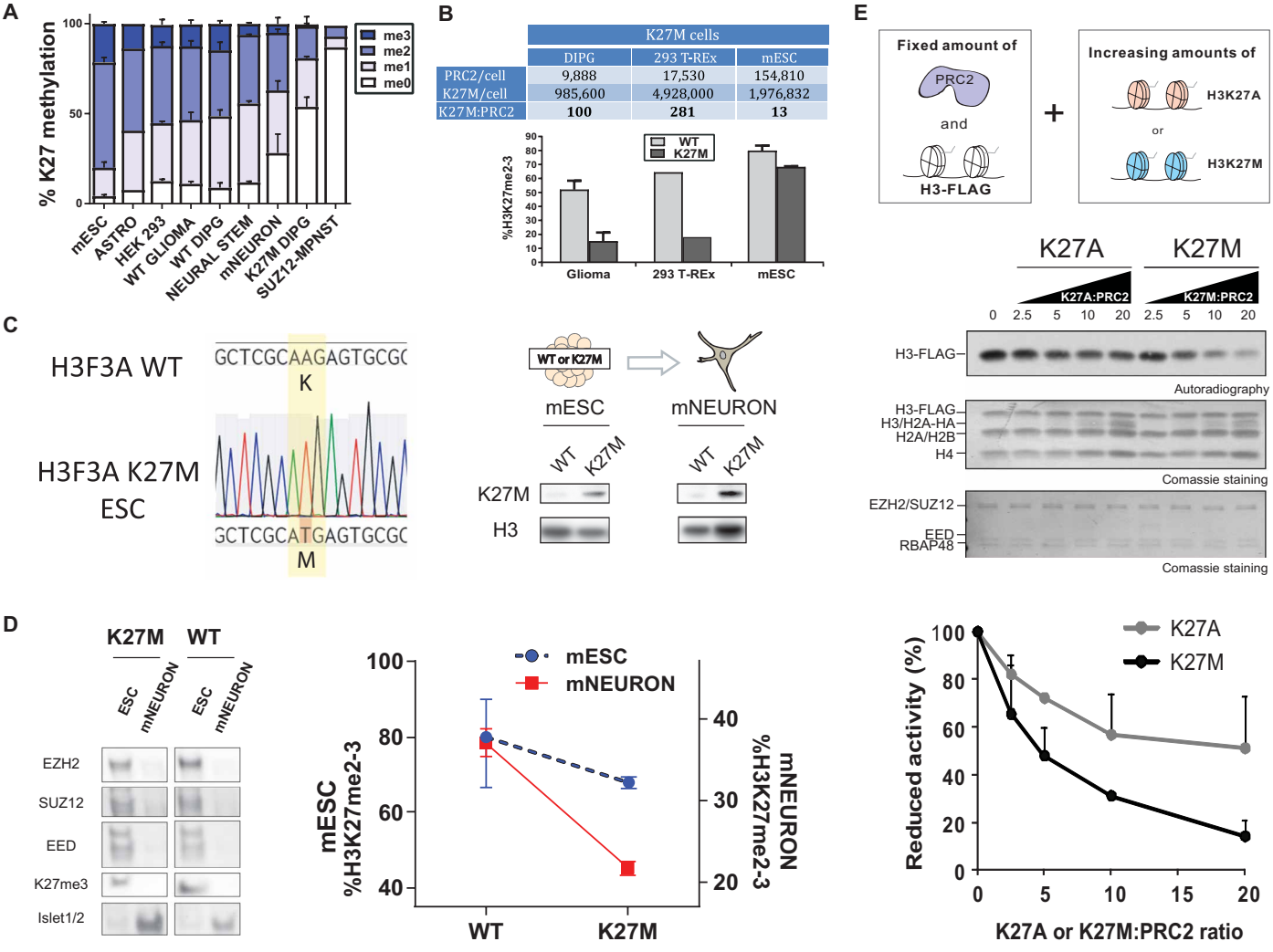

Fig. 1. PRC2 inhibition as a function of the H3K27M-to-PRC2 ratio. (**A**) Samples are ranked left to right based on levels of H3K27me2-3, as detected by mass spectrometry (MS). mESC, mouse embryonic stem cell ($n = 2$); ASTRO, human astrocyte ($n = 1$); HEK 293, human embryonic kidney 293 cells ($n = 2$); WT GLIOMA, H3K27WT cortical glioma ($n = 4$); WT DIPG, H3K27WT DIPG ($n = 2$); NEURAL STEM, human neural stem cells ($n = 2$); mNEURON, mouse motor neuron ($n = 3$); K27M DIPG, DIPG with H3K27M ($n = 2$ for H3.1K27M and $n = 2$ for H3.3K27M); SUZ12-MPNST, malignant peripheral nerve sheath tumor that is SUZ12 null ($n = 1$). (**B**) PRC2 molecules per cell (average of EED, EZH2, and SUZ12) were determined by quantitative MS and are presented in the table, along with the relative ratio of H3K27M to PRC2. Levels of H3K27me2-3 determined by MS are presented in the chart below. DIPG and 293 T-REx cells with a large excess of K27M to PRC2 showed the most robust attenuation of H3K27me2-3 levels, while embryonic stem cells (mESC) with a more modest excess of K27M (~13-fold) showed a less robust loss in K27me2-3 relative to their WT counterparts (see table S1 for cell line details and fig. S1 for cell lines used in PRC2 quantitation analyses). (**C**) mESCs generated using CRISPR harboring either WT or a K27M mutation at H3F3A were differentiated to motor neurons (mNEURONs). Left: Sanger sequencing results for H3F3A K27M mESCs compared with WT mESCs. Right: Western blot validating the cell lines by H3K27M protein expression. (**D**) Left: Western blot validating the cell lines and increased K27M expression with significantly reduced levels of PRC2 core components in mNEURON. Islet1/2 served as an mNEURON marker. Right graph: Differentiation to mNEURON led to decreased K27me2-3 in K27M cells, relative to their mESC precursors, as measured through MS ($n = 2$ per cell type). (**E**) Top: Histone methyltransferase (HMT) assays containing PRC2 and increasing ratios of 8× oligonucleosomes comprising H3K27A or H3K27M and hemagglutinin (HA)–tagged H2A. Substrate oligonucleosomes were distinguishable by their reconstitution with H3-FLAG. Middle: Representative HMT assay shows levels of methylation and relative concentration of each HMT component. Bottom: Graphs quantitate the relative amount of ^{3}H-SAM incorporated into histone H3-FLAG. Higher H3K27M-to-PRC2 ratios produce larger deficits in PRC2 activity ($n = 3$ per data point). Data plotted as means ± SD.

active regions in both the isogenic K27M 293 T-REx and K27M DIPG cells themselves (fig. S2B) suggests a dynamic environment wherein histone modifications associated with transcription activity [this study and (*6*, *13*)], histone turnover (*23*), and even nascent mRNA might lead to the failure of K27M to stably recruit PRC2 [i.e., the eviction of PRC2 (*11*, *24*)]. While we cannot exclude the possibility that the release of PRC2 from H3K27M arises from a more direct effect on PRC2 itself (see Discussion), we expect that future studies will find that the interaction and release of PRC2 from H3K27M are determined by the interplay between the local chromatin environment and structural changes to PRC2 itself.

Persistent inhibition of PRC2 after its dissociation from H3K27M

We next sought to better understand the impact of H3K27M on PRC2 activity at more typical PRC2 target sites. First, we identified

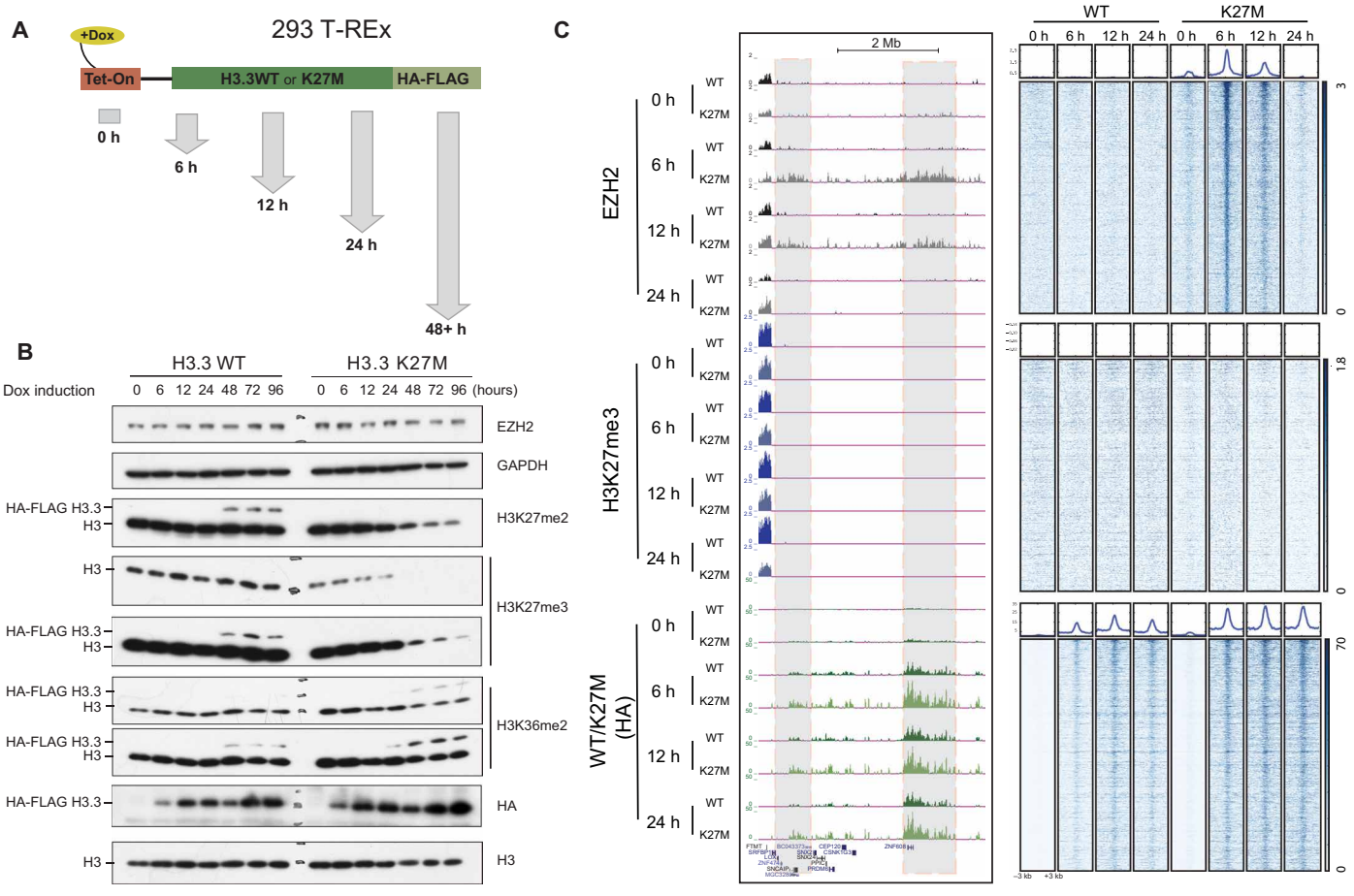

Fig. 2. Abnormal recruitment and release of PRC2 from H3K27M-containing chromatin. (**A**) 293 T-REx cells were induced to express C-terminal, FLAG-HA–tagged H3.3K27M (K27M) or FLAG-HA–tagged H3.3K27WT (WT) during the indicated time course. Dox, doxycycline. (**B**) Western blots revealed the progressive loss in H3K27me2-3 and gain of H3K36me2 as a function of time of H3.3K27M expression (note the slower migration of tagged H3.3 versions). GAPDH, glyceraldehyde-3-phosphate dehydrogenase. (**C**) Left: ChIP-seq for EZH2, H3K27me3, and HA-tagged WT/K27M histones performed at select time points and displayed as representative enrichment tracks. EZH2 peaks detected exclusively under the 6- and 12-hour conditions in K27M-expressing cells are highlighted in gray. Right: Heatmaps were generated by centering and rank ordering the 6-hour EZH2 peaks detected within EZH2 regions present only at the early 6- and 12-hour time points (1450 domains, 2325 peaks). Corresponding average density profiles are plotted at the top of the heatmaps. Peaks occurring specifically at the early time points (6- and 12-hour time points) strongly colocalize with K27M, are unique to the K27M cells, and are depleted by 24 hours.

616 broad PRC2 (EZH2) domains present in both H3K27M and H3K27WT cells across all time points and found that, despite the retention of EZH2 at a subset of genes at 24 hours in H3K27M cells, a global loss of H3K27me3 was evident (Fig. 3A and fig. S3 for visualization of the broad domains). As the cells progressed, attaining steady-state levels of H3K27M, the loss in H3K27me3 was even greater in magnitude, despite the retention of EZH2 and the lack of H3K27M enrichment at those same sites after 72 hours of H3K27M expression (Fig. 3B). Together, these results are consistent with recent work showing that loci depleted of H3K27me3 in H3K27M cells have equal PRC2 occupancy and with emerging evidence that PRC2 recruitment can be uncoupled from its enzymatic activity [(*5*, *25*) and see below].

We next investigated whether the interaction of PRC2 with H3K27M-containing nucleosomes might have a lasting impact on its function. This was motivated by our observations (i) that newly expressed K27M deposits at sites that are not usually regulated by PRC2 and PRC2 are transiently recruited at these new sites and (ii) that some PRC2-regulated genes maintain PRC2, but its activity is reduced in H3K27M cells (Figs. 2 and 3). To study this, we expressed tagged PRC2 in H3K27M- and H3K27WT-expressing 293 T-REx cells (fig. S4, A and B). PRC2 was then purified using a combination of conventional and tandem affinity chromatography, yielding PRC2 in correct stoichiometry between samples (Fig. 4A). H3K27M was not detected by Western blotting and MS analysis in the purified PRC2 fractions (Fig. 4A and fig. S4C). We found that the catalytic activity of PRC2 purified from H3K27M-expressing cells was markedly decreased relative to PRC2 purified from H3K27WT cells and that this inhibition was SAM dependent (Fig. 4B), which is consistent with the previous observation demonstrating that SAM is necessary for inhibition of the methyltransferase by K-to-M mutation on histone H3 (*26*). This lasting H3K27M inhibitory effect on PRC2 was also observed using a system reconstituted with all recombinant components, including PRC2 comprising only its four core subunits (EZH2, EED, SUZ12, and RBAP48; Fig. 4C) and oligonucleosomes formed with bacterially expressed histones (Fig. 4D). After release from H3K27M-containing oligonucleosomes, the resultant PRC2 was generally less active (Fig. 4E), in line with a widespread attenuation of H3K27me2-3 in K27M DIPG. Given that lasting PRC2

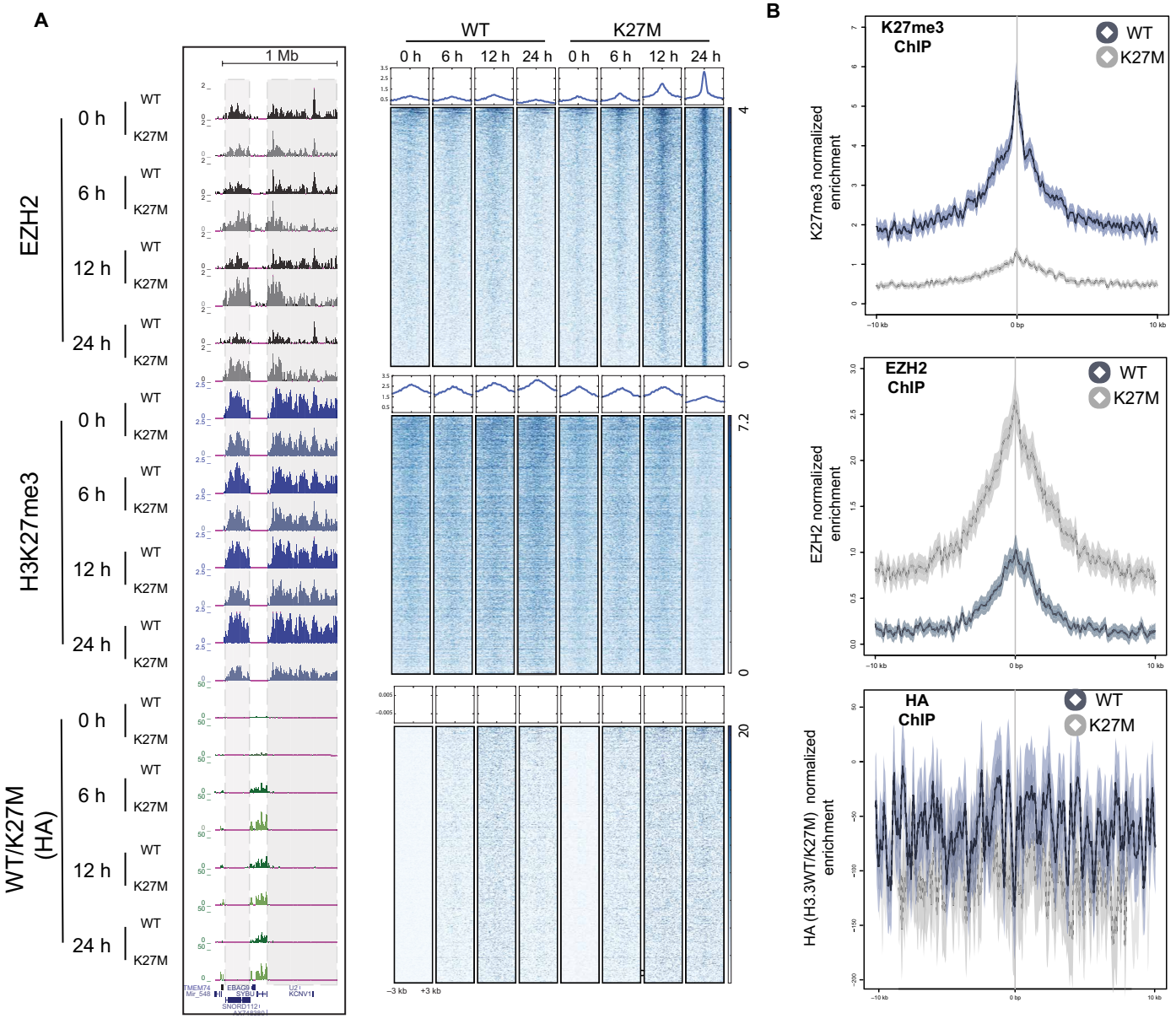

Fig. 3. PRC2 is recruited to normal target sites but is progressively less active on chromatin following H3K27M expression. (**A**) ChIP-seq for EZH2, H3K27me3, and HA-tagged WT/K27M histones performed at select time points and displayed as representative enrichment tracks (left). PRC2 (EZH2) domains detected in both WT- and K27M-expressing cells across all time points are highlighted in gray. Right: Heatmaps centering on the 24-hour EZH2 peaks within the common PRC2 domains (616 domains, 2253 peaks) indicate strong EZH2 enrichment at that time point, decreased H3K27me3, and little detectable co-enrichment with H3K27M (HA). NTA, nitrilotriacetic acid. (**B**) To confirm the effects at the 24-hour time point, ChIP-seq was performed after 72 hours of H3.3K27M (K27M) and H3.3K27WT (WT) expression for EZH2, HA, and H3K27me3. Genome-wide enrichment plots centered on the common EZH2 domains corresponding to those in (A) are presented. Despite a loss in H3K27me3 in H3K27M cells relative to WT (top), EZH2 occupancy is increased, and the tagged histones are not enriched (middle and bottom, respectively). bp, base pair.

inhibition is seen in vivo and within a fully recombinant system, we speculate that H3K27M-containing chromatin alters the core PRC2 complex through a stable conformational change (see Discussion).

Inhibition of allosteric activation of PRC2 and spreading of H3K27me3

We noted a strong similarity between the phenotype of H3K27M cells in which PRC2 is recruited but exhibits diminished activity and that of PRC2 mutants that are deficient in allosteric activation (*25*). Thus, we next tested whether H3K27M may preferentially impair allosteric activation of PRC2. To accomplish this, we incubated PRC2 with increasing amounts of the allosterically activating H3K27me3 peptide in the presence of SAM and nucleosomes comprising either H3K27M or control H3K27A (HA-tagged H2A; Fig 5A). PRC2 activity was subsequently assessed by adding WT nucleosomes (distinguished by a C-terminal FLAG-tagged H3; Fig. 5A). Strikingly, while there was little difference in the absence of H3K27me3 peptide, PRC2 was refractory to stimulation by

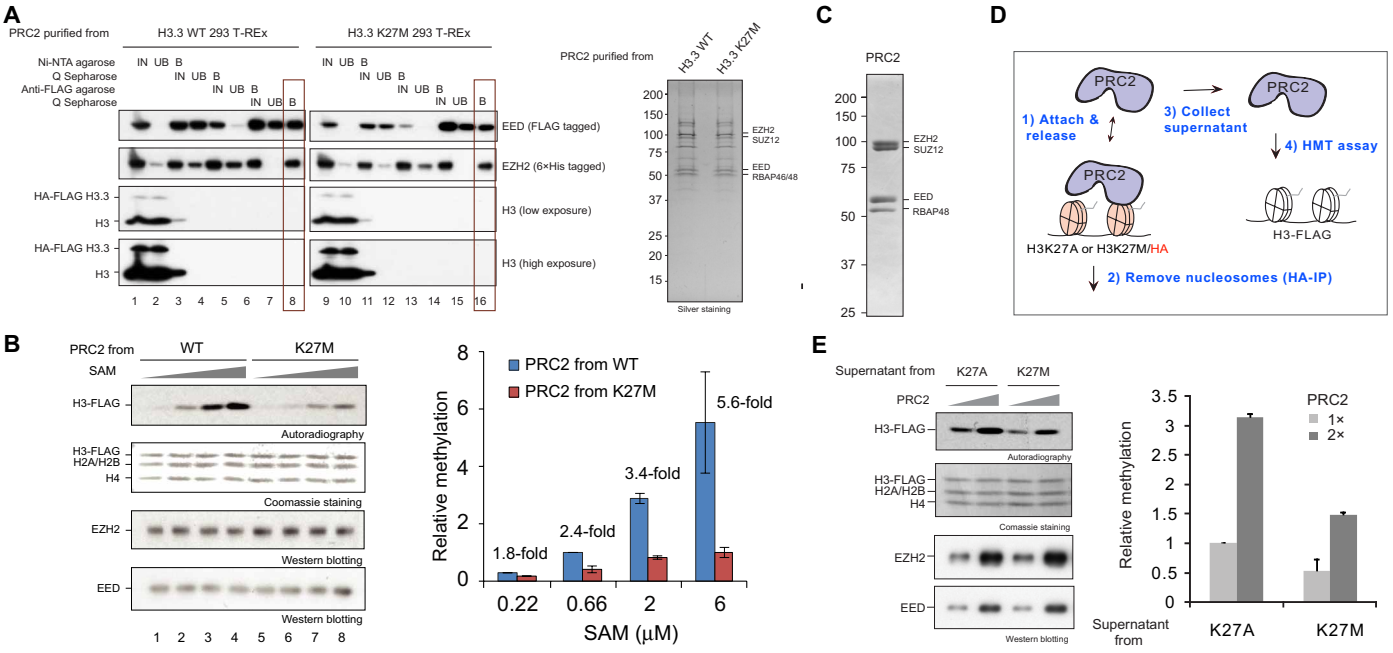

Fig. 4. PRC2 purified from H3K27M cells or nucleosomes is less active. (**A**) PRC2 containing 6×His-tagged EZH2 and FLAG-tagged EED was purified from 293 T-REx cells expressing H3.3K27M or H3.3K27WT for 3 days. Left: Western blot of levels of EZH2, EED, and histone H3 at each purification step. Note that histones and nonstoichiometric levels of EED or EZH2 were well removed through purification (see also fig. S4). IN, input; UB, unbound; B, bound. Lanes 8 and 16 (boxed) represent the final, purified PRC2 complex used in subsequent assays. Right: Silver staining showing the relative purity of each purified PRC2 complex. (**B**) Left: Purified PRC2 complexes as in (A) were subjected to HMT assays using 8× oligonucleosomes with H3-FLAG as substrate (300 nM) and increasing amounts (0.22, 0.66, 2, and 6 μM) of SAM [^{3}H-SAM:SAM (1:9)]. Right: Quantification of the relative amounts of ^{3}H-SAM incorporated into histone H3-FLAG substrate (n = 2). Data are plotted as means ± SD. (**C**) Coomassie blue staining shows recombinant PRC2 (EZH2, EED, SUZ12, and RBAP48) purified from SF9 cells. (**D**) Schematic representation of the method used to recover recombinant PRC2 after its association with different types of recombinant chromatin. Recombinant PRC2 (15 and 30 nM) was initially incubated with 8× oligonucleosomes containing HA-tagged H2A and either H3K27A or H3K27M (300 nM) for 1 hour at 30°C. PRC2 was then recovered by HA immunoprecipitation (IP), and the supernatant was collected. Equal amounts of unbound PRC2 (1× or 2×) was incubated with ^{3}H-SAM (500 nM) using 8× oligonucleosomes comprising H3-FLAG as substrate (300 nM). (**E**) Left: A representative image of the HMT assays. Right: Quantitation of relative amount of ^{3}H-SAM incorporated into histone H3-FLAG substrate (n = 3). Data are plotted as means ± SD.

H3K27me3 in the presence of H3K27M nucleosomes (Fig. 5B). Furthermore, the presence of H3K27me3 selectively increased the binding affinity of PRC2 toward H3K27M-containing chromatin (Fig. 5C). Combined, these results indicate that the allosterically activated form of PRC2 (*25*, *27*) binds stronger to H3K27M and that PRC2 catalysis is more sensitive to H3K27M.

To examine whether a similar defect in catalysis exists in H3K27M-bearing glioma, we used an internal spike-in normalized ChIP-seq protocol and directly compared H3K27me3 deposition in two independent H3K27M DIPG and H3K27WT glioma cell lines (selected on the basis of being pediatric World Health Organization grade IV, matched culture conditions, and IDH1 WT). The H3K27me3 peaks in the H3K27M cells appeared sharper and larger in magnitude than those observed in WT cells (Fig. 5D, left). Genome-wide analysis confirmed these observations, and more importantly, revealed that the "remaining" H3K27me3 peaks in H3K27M glioma were not subject to spreading into large repressive H3K27me-containing domains as observed in WT cells, a process likely dependent on PRC2-mediated allosteric activation (Fig. 5D, right) (*25*, *27*). Our results are consistent with a broader mechanism of K-to-M substitutions, as evidenced in *Schizosaccharomyces pombe*, wherein H3K9M induces a gain in H3K9me3 and its methyltransferase (Clr4) at H3K9me3 nucleation sites, while H3K9me3 spreading across domains is lost (*16*). Our results account for the recent descriptions of H3K27M isogenic and glioma cells wherein there is a focal gain in H3K27me3 at previously established PRC2 target loci that are CpG island dense (*5*, *7*, *8*, *12*). Thus, by impairing allosteric activation of PRC2, and hence spreading H3K27me3 (*25*, *27*), H3K27M achieves both a global loss of H3K27me3 and a focal accumulation of H3K27me3 at PRC2 recruitment sites.

Altered histone modification landscape in H3K27M DIPG

Given the widely documented cross-talk among histone modifications, we tested whether the presence of H3K27M might affect the global histone modification landscape that could further affect PRC2 activity, resulting in an aberrant epigenetic profile in DIPG. In H3K27M-bearing DIPGs, a few histone modifications such as H3K27 acetylation have already been shown to increase in concert to the decrease in H3K27me3 (*3*, *4*, *12*, *28*). However, a systematic analysis of the histone modification profile of DIPGs has so far been hampered, perhaps by the scarcity of suitable WT controls, given that most of DIPGs carry the H3K27M mutation. Here, we were able to use the same quantitative histone modification MS approach as above on a panel of human primary H3K27WT glioma cell lines, two different H3K27WT DIPGs, and four different H3K27M DIPGs to identify global histone modification alterations against a relevant control background. Consistent with other studies was a large-scale gain of histone acetylation in H3K27M DIPG (fig. S5). However, we observe that the largest gain of acetylation is on the H4 tail (~20% gain). This finding suggests that histone acetylation events beyond

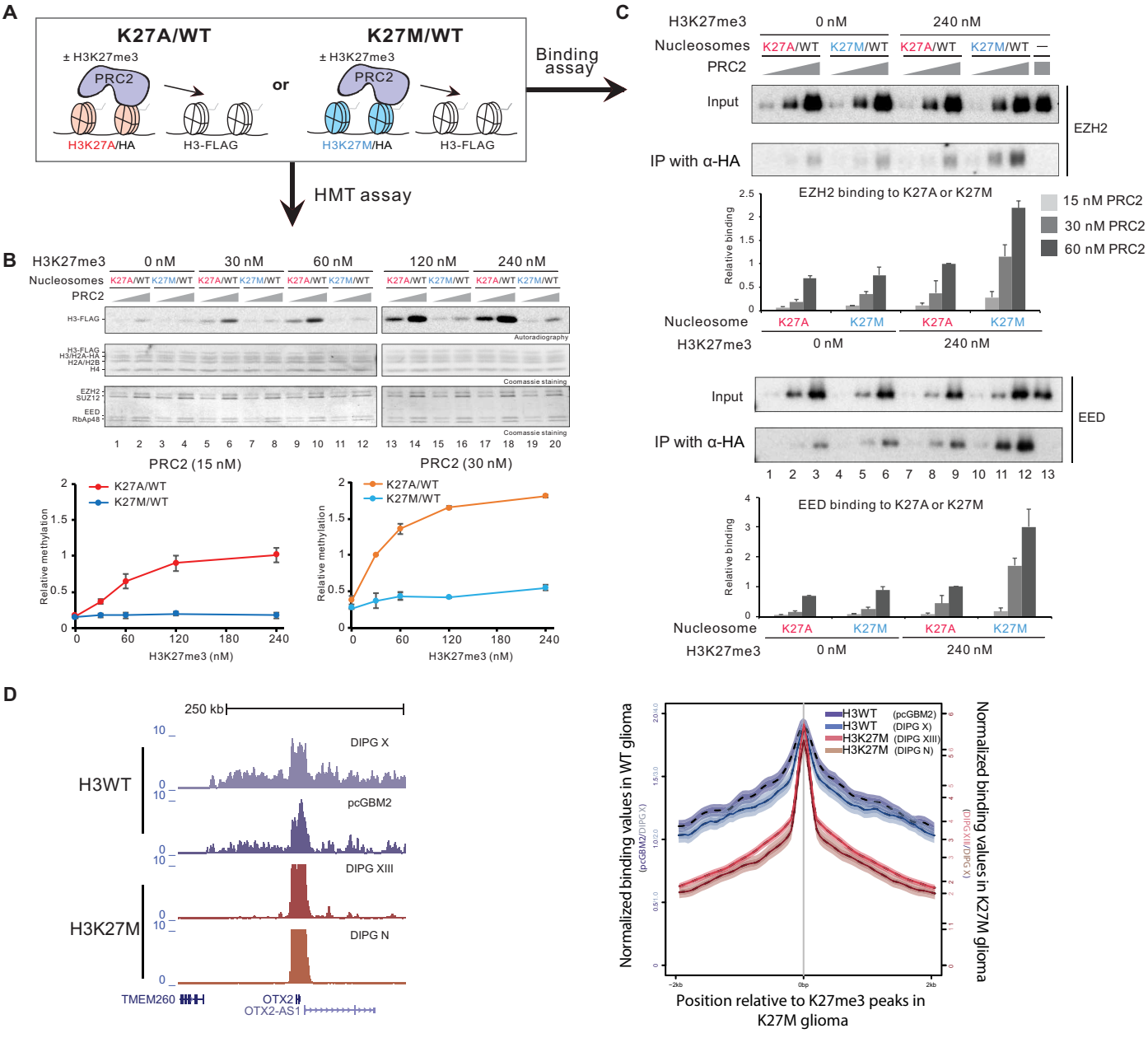

Fig. 5. H3K27M preferentially inhibits allosterically activated PRC2 in vitro and restricts remaining H3K27me3 in DIPG. (**A**) Schematic representation of experiments in which PRC2 was incubated with ^{3}H-SAM, increasing concentrations of H3K27me3 peptide, and 12× oligonucleosomes comprising HA-tagged H2A and either H3K27A or H3K27M. Oligonucleosomes containing FLAG-tagged H3 (300 nM) were added as a substrate. (**B**) One-half of the reaction was subject to autoradiography with subsequent quantification of the relative amount of ^{3}H-SAM incorporated into the FLAG-tagged histone H3 (n = 3 per data point). Data are plotted as means ± SD. (**C**) The other half of the reaction was used to measure the amount of PRC2 retained on H3K27M- versus H3K27A-containing 12× nucleosomes by Western blot for EZH2 and EED after immunoprecipitation of the HA-tagged H2A-containing oligonucleosomes. The band intensity of EZH2 or EED served as a readout of EZH2 bound or EED bound on H3K27M- or H3K27A-containing 12× oligonucleosomes, as indicated (n = 3 per data point). Data are plotted as means ± SD. (**D**) Left: Representative H3K27me3 ChIP-seq tracks from patient-derived glioma cell lines with K27M (n = 2 cell lines) or WT H3 (n = 2 cell lines), showing very sharp, narrow peaks in the K27M glioma and much broader peaks in the WT glioma. Right: Genome-wide trend plot indicating that the remaining K27me3 peaks in the K27M glioma are more punctate in contrast to the WT glioma that show large, broad H3K27me3 signal indicative of typical polycomb domains.

the relatively smaller net gain in H3K27 acetylation (~0.3%) reported here (fig. S5) and elsewhere (*3*, *6*, *29*) might be important drivers of the disease.

The most marked result was a significant gain in H3K36me2 within H3K27M DIPG cells (Fig. 6A). ChIP-seq indicated higher levels of H3K36me2 on H3K36me2 target genes in K27M DIPG relative to WT (Fig. 6, B and C). In our isogenic H3K27M 293 T-REx system, we further observed an invasion of H3K36me2 largely into former PRC2 domains that lost H3K27me3 (fig. S6). These alterations in the euchromatic H3K36me2 domains and the corresponding

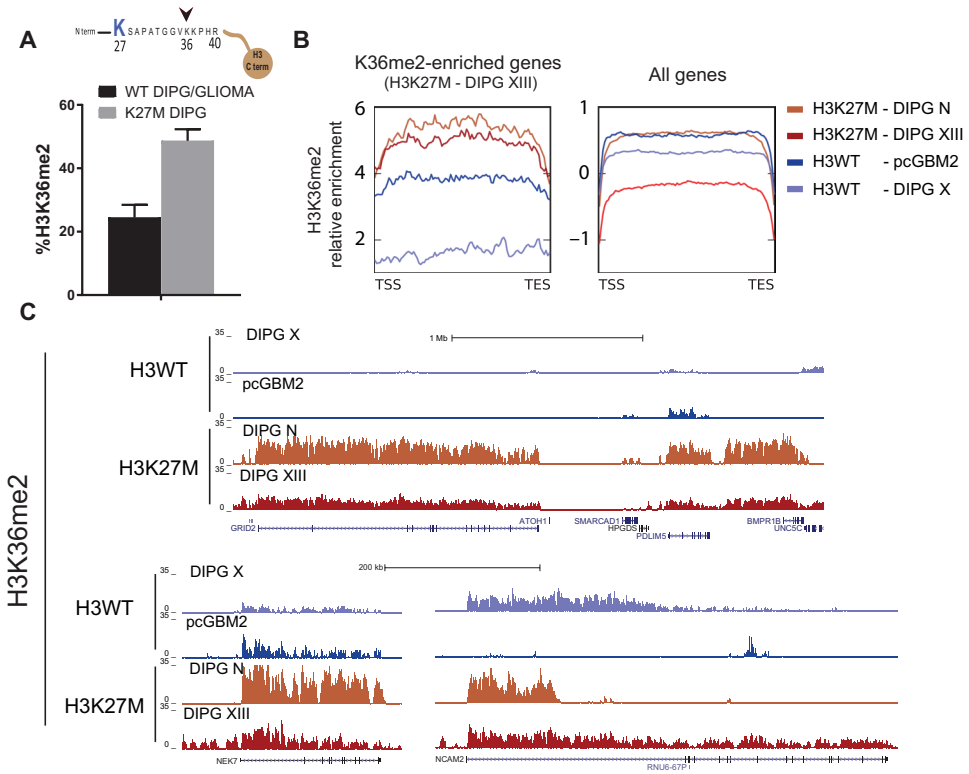

Fig. 6. Gain of K36me2 in H3K27M DIPG. (**A**) H3K36me2 levels are significantly higher in H3K27M DIPG ($n = 2$ for H3.1K27M and $n = 2$ for H3.3K27M) than in WT DIPG/GLIOMA ($n = 4$ for H3K27WT cortical glioma and $n = 2$ for H3K27WT DIPG), as revealed by MS (see fig. S7). Data are plotted as means ± SD. (**B**) H3K36me2 ChIP-seq performed with glioma cell lines bearing either WT histone H3 ($n = 2$ total) or H3K27M, as indicated ($n = 2$; see table S1 for details). Left: The trend plot was generated by first identifying genes that displayed significant H3K36me2 enrichment above input for the H3K27M-bearing DIPG XIII cell line (1727 genes). Subsequently, average H3K36me2 levels were plotted for each glioma cell line across those genes (transcriptional start to end site). Right: As a control, H3K36me2 was plotted over all genes in the genome. Combined, H3K36me2-enriched genes in the H3K27M DIPG showed overall higher levels of H3K36me2 relative to glioma with WT histone H3. (**C**) Representative ChIP-seq tracks show generally elevated levels of H3K36me2 across these genes in H3K27M DIPG. Variations of the effect can be seen in these gliomas: Some genes are devoid of H3K36me2 in H3WT gain H3K36me2 in H3K27M, while others contain H3K36me2 in both H3WT and H3K27M glioma, yet the levels in the H3K27M cell lines are generally higher. TSS, transcriptional start site; TES, transcriptional end site.

heterochromatic H3K27me3 domains are reminiscent of sarcoma cells that express H3K36M and exhibit dampened H3K36 methyltransferase(s) activity, leading to abnormal deposition of H3K27me3 (*30*). Because of the heterogeneity of pediatric glioma culture cell lines, we selected a WT (DIPG X) and a K27M (DIPG XIII) cell line to compare by RNA sequencing (RNA-seq), as these are better matched with respect to both being DIPG, as well as their growth properties as nonadherent tumorspheres. As expected, the regions that gain H3K36me2 in K27M DIPG also show up-regulation of those genes (fig. S7A) and are associated with proneuronal phenotypes, cancer pathways, and cell adhesion phenotypes seen in H3K27M DIPG by KEGG (Kyoto Encyclopedia of Genes and Genomes) pathway analysis (fig. S7B). Thus, in each of these cases, the K-to-M mutations disrupt heterochromatic and euchromatic domains that have potential to drive aberrant gene expression patterns important for proliferation, cancer stem cell properties, and oncogenesis (*4*–*7*).

DISCUSSION

A primary challenge in the H3K27M field has been to resolve the contradictory observations indicating that PRC2 has a high affinity for H3K27M peptides, yet PRC2 and H3K27M are often mutually excluded from chromatin in H3K27M DIPG (*4*, *6*, *9*, *10*). Our studies revealed that interaction of H3K27M with PRC2 is a dynamic process that cannot be captured by static, steady-state approaches. Namely, there is an initial phase after H3K27M is expressed and incorporated into chromatin, followed by PRC2 recruitment to H3K27M-containing chromatin, presumably due to its higher affinity toward H3K27M (Fig. 2C). However, in the next phase, PRC2 is released from H3K27M, as they do not colocalize at steady-state conditions in both isogenic 293 T-REx systems (e.g., this study, Figs. 2 and 3) and the H3K27M DIPG themselves (*6*). This dynamic model therefore accommodates both the finding of high H3K27M and PRC2 affinity in select assays and their failure to be stably colocalized on chromatin in cells. In line with the more fluid effect of H3K27M is a recent high-resolution imaging study suggesting that, although H3K27M does not change the amount of PRC2 bound to chromatin, it can increase the time needed for PRC2 to find and select its target chromatin loci (*31*). An implication of these studies is that PRC2 is not stable on H3K27M-containing chromatin, an effect with marked resemblance to the recently proposed "hit and run" hypothesis of PRC2, where core PRC2 devoid of "stabilizing" components such as MTF2 and JARID2 is less stable on chromatin (*27*). These findings therefore set the stage for future proteomic studies designed to test whether PRC2 might exhibit a decreased association with these stabilizing cofactors, whether the PRC2 core complex is subjected to

other more direct effects through its association with H3K27M, and/or whether there is a rapid change in the epigenome by the gain of H3K36me2 (this study) and H3K27ac (*6*).

One of the most unexpected findings in our study was a second, previously unknown mode of PRC2 inhibition that apparently persists even after its dissociation from H3K27M (Fig. 4). This mode of inhibition was more severe as the concentration of SAM increased, suggesting that the PRC2 bound and/or released from K27M might have a defect in SAM turnover, thereby delaying catalysis (*9*). The other possibility is that H3K27M might inhibit EZH2 automethylation (*32*, *33*), eventually influencing the activity of PRC2 on chromatin. Recent studies from our group and others revealed novel automethylation sites on EZH2 and highlighted the impact of EZH2 automethylation on PRC2 activity (*32*, *33*). It is intriguing to speculate that EZH2 automethylation could stably change the conformation of the PRC2 complex, thereby altering its activity on chromatin. Seemingly, in line with a lasting effect of H3K27M on PRC2 is a recent study showing that, while the levels of PRC2 bound to chromatin do not change, the search time of PRC2 for chromatin is increased in cells that express H3K27M (*31*). While other variables such as lower H3K27me3 levels may affect PRC2 search time, it is consistent with our findings that there may be a lasting change in PRC2 following its dissociation from H3K27M-containing chromatin that affects its later function.

Our mechanistic studies were also able to give insight into the paradoxical observation that, despite a widespread loss in H3K27me3, there are a smaller number of loci that actually gain H3K27me3 in DIPG at steady state (*4*, *5*, *7*, *12*). We showed that H3K27M has a strong inhibitory effect on the allosterically activated form of PRC2 (Fig. 5), an effect similar to the one previously reported using structural studies (*9*). To put our finding in the context of the current literature, the initial step of allosteric activation of PRC2 is its binding to H3K27me3, the terminal enzymatic product of PRC2, through its essential EED subunit. The result is a conformational change in EZH2 that stabilizes its catalytic SET domain, leading to a substantial enhancement of its HMT activity (*9*, *34*). This positive feedback loop facilitates the spreading of H3K27me2-3 from PRC2 recruitment sites (*27*, *35*). We postulate that the allosterically activated form of PRC2 preferentially binds H3K27M and then becomes less active; however, it is still recruited to strong polycomb loci in H3K27M cells. This less active version of PRC2 would be much less efficient at spreading H3K27me3 (*25*), leading to a global loss of H3K27me3-decorated repressive domains. Yet, the less catalytically active PRC2 might still accumulate at those polycomb foci, leading to an overall gain in the focal concentration of H3K27me3 at steady state. This hypothesis is in keeping with the gain of H3K27me3 at select regions, despite the more global loss in PRC2 activity.

In the context of the broader chromatin landscape in H3K27M, we showed both large gains in histone acetylation (fig. S5), as previously reported (*3*, *6*, *12*), and the novel and robust increase in another histone modification associated with transcription, H3K36me2 (Fig. 6). On the basis of the recent studies suggesting that disrupting the balance of PRC2 activity and H3K36me levels can drive oncogenesis, we speculate that high H3K36me2 levels might represent a core feature of H3K27M DIPG (*30*). Note that, given the heterogeneity present within H3K27M DIPG compared to H3WT glioma, more work is needed to better understand the precise contributions of H3K36me2 to transcriptional programs that might drive oncogenesis, specifically in H3K27M DIPG. These studies of the downstream effects of H3K36me2 will likely be fruitful since readers of this modification, as well as the enzymes that place this modification, are potentially drugable therapeutic vulnerabilities in DIPG. Targeting oncogenic chromatin features, such as residual PRC2 activity as well as the gain of histone acetylation marks and their readers, has been shown to decrease the hallmarks of DIPG growth and aggression in preclinical models (*2*, *5*, *6*, *29*, *36*). Therefore, combining biochemistry with mechanistic studies, proteomics, and DIPG disease model systems promises not only to shed light on the underlying biology but also to reveal novel targets, alone or in combination, for therapeutic intervention in this otherwise intractable disease.

MATERIALS AND METHODS

Cell culture models and tissue preparation

A complete list of cell lines and in vivo H3K27M model systems can be found in table S1. Culture methods are briefly described below.

Mouse stem cells and mNEURON differentiation

E14 mESCs were cultured as described previously (*17*). Differentiation to cervical mNEURONs is detailed in (*17*), but briefly, ESCs were plated at low density in the absence of mitogenic factors to form embryoid bodies. Two days later, media were supplemented with 1 μM retinoic acid and 0.5 μM smoothened agonist. Cells were harvested 4 days later, with one media replenishment for 2 days.

Human brain tumor models

Patient-derived glioma cell lines, including DIPG cell lines (see table S1 for source), were cultured in tumor stem cell media as described (*37*, *38*). Human neural stem cells were derived and cultured as described previously (*39*). New York University (NYU) patient–derived tumor cell line generation has been approved by the NYU Institutional Review Board (IRB) (no. S15-01228). Pathological diagnoses of primary tumors, from which cell lines were derived, were performed by a board-certified neuropathologist (M.S.), and molecular characteristics were established at an NYU Clinical Laboratory Improvement Amendment (CLIA)–certified molecular pathology laboratory. Furthermore, relevant tumor sample collection and molecular profiling were approved by the NYU IRB (nos. S12-00865 and S14-00948, respectively). All human tumor samples were reviewed, and diagnosis was performed by a board-certified neuropathologist (M.S.) in a CLIA-certified pathology laboratory.

Generation of isogenic cell lines

mESC model

The H3K27M mutation was introduced into the H3F3A locus through CRISPR-Cas9 engineering as described in (*17*). Briefly, guide RNA (gRNA) directed at H3F3A were designed using the tool (http://crispr.mit.edu/design) and cloned into the SpCas9-2A-GFP vector (plasmid no. 48138, Addgene). mESCs were cotransfected with the Cas9, gRNA, and donor DNA template to promote homology-directed repair, resulting in an M substitution at K27 of H3F3A (i.e., AAG to ATG). Cells containing the Cas9 vector were selected by green fluorescent protein (GFP) and fluorescence-activated cell sorting (FACS), and single cells were plated at low density. Individual colonies were picked 5 to 7 days later. Individual clones bearing the mutation were harvested and genotyped using Sanger sequencing. Colonies positive for the H3F3A K27M substitution were passaged at least five times to confirm purity of the population.

293 T-REx model

Cells were cultured using standard media (Dulbecco's modified Eagle's medium + fetal bovine serum + metabolic support). Stable cell lines

in which the expression of the integrated transgene, either H3.3K27WT or H3.3K27M, under the control of doxycycline were generated by transfecting pINTO-NFH vector (*40*). Stable cell lines were selected using zeocin-selectable (200 μg/ml) and blasticidin-selectable (10 μg/ml) markers encoded in the pINTO-NFH vector. Stable integration was subsequently confirmed by Sanger sequencing. To induce expression of the H3.3K27WT or H3.3K27M transgenes, doxycycline (1 μg/ml) was added at the appropriate time point before harvesting.

A derivative of 293 T-REx suitable for PRC2 purification was generated as follows. A 6×His-tagged EZH2 complementary DNA (cDNA) and FLAG-tagged EED cDNA were subcloned into the pLVX-EF1α-IRES-mCherry lentiviral vector (Clontech). Cells stably expressing both 6×His-tagged EZH2 and FLAG-tagged EED cDNAs were generated by lentiviral transduction. For the production of viral particles, lentiviral vectors were cotransfected with pcREV, BH10, and pVSV-G into 293 T-REx cells. The virus-containing medium was collected 48 hours after transfection. The viruses carrying 6×His-tagged EZH2 or FLAG-tagged EED were mixed in a 1:1 ratio before infection of 293 T-REx cells. Polybrene was added to the viral medium at a concentration of 8 μg/ml. Infected cells were selected using mCherry expression by FACS.

Purification of recombinant proteins

To purify the human PRC2 core complex, FLAG-tagged EED, 6×His-tagged EZH2, SUZ12, and RBAP48 were cloned into the baculovirus expression vector pFASTBac1 (Invitrogen). Recombinant PRC2 was produced in SF9 cells grown in SF-900 III SFM (Invitrogen). After 60 hours of infection, SF9 cells were resuspended in BC150 [25 mM Hepes-NaOH (pH 7.8), 1 mM EDTA, 150 mM NaCl, 10% glycerol, and 1 mM dithiothreitol (DTT)] with 0.1% NP40 and protease inhibitors [1 mM phenylmethylsulfonyl fluoride (PMSF), 1 mM benzamidine, pepstatin A (1 μg/ml), leupeptin (1 μg/ml), and aprotinin (1 μg/ml)]. Cells were lysed by sonication (Sonic Dismembrator model 100, Fisher Scientific), and PRC2 complexes were purified through Ni-NTA agarose beads (Qiagen), FLAG-M2 agarose beads (Sigma-Aldrich), and Q Sepharose beads (GE Healthcare).

Purification of PRC2 from 293 T-REx

After expressing H3.3K27M or H3.3K27WT using doxycycline (1 μg/ml) for 72 hours, cells grown in plates (40 cm by 15 cm) were harvested for each condition. Nuclei were purified using a standard hypotonic lysis approach, and nuclear extract was prepared using BC400 buffer [20 mM tris (pH 7.9), 400 mM KCl, 0.2 mM EDTA, 0.5 mM DTT, 20% glycerol, 0.05% NP-40, 1 mM PMSF, 1 mM benzamidine, pepstatin A (1 μg/ml), leupeptin (1 μg/ml), and aprotinin (1 μg/ml)]. The first purification step used Ni-NTA agarose beads to purify EZH2 that had a 6×His tag, followed by Q Sepharose. The eluate was then further purified using FLAG-M2 agarose beads to isolate the complex containing FLAG-tagged EED, followed by another Q Sepharose. PRC2 was eluted in BC500 [20 mM Hepes-NaOH (pH 7.8), 500 mM NaCl, 0.02% NP-40, 10% glycerol, 1 mM PMSF, and 1 mM benzamidine]. Components of purified PRC2 were visualized by silver staining after SDS–polyacrylamide gel electrophoresis (PAGE), and its activity was gauged in HMT assays. PRC2 was also purified from 293 cells containing FLAG-tagged EED, but not 6×His-tagged EZH2, using FLAG-M2 agarose and Q Sepharose.

Nucleosome reconstitution

Purification of recombinant histones, refolding recombinant octamers, and reconstitution of nucleosomes were generated as described previously (*25*).

HMT assay

Standard HMT assays were performed as described (*25*), unless otherwise stated in the figure legends. Briefly, the reaction was performed in a total volume of 15 μl of HMT buffer [50 mM tris-HCl (pH 8.5), 5 mM $MgCl_2$, and 4 mM DTT] with the indicated amounts of recombinant human PRC2 complex (EZH2, EED, SUZ12, and RBAP48), 500 nM of ^{3}H-labeled SAM (PerkinElmer). Specific conditions related to the main figures are presented below with the supplementary figures' detailed information provided.

All reaction mixtures were incubated for 60 min at 30°C and stopped by the addition of 4-μl SDS buffer [0.2 M tris-HCl (pH 6.8), 20% glycerol, 10% SDS, 10 mM β-mercaptoethanol, and 0.05% bromophenol blue]. After HMT reactions, samples were incubated for 5 min at 95°C and resolved on SDS-PAGE gels. The gels were then subjected to Coomassie blue staining for protein visualization or wet transfer of proteins to 0.45-μm polyvinylidene difluoride (PVDF) membranes (Millipore). The radioactive signals were detected by exposure on autoradiography films (Denville Scientific).

PRC2 quantitation by MS

Cell lysate preparation

Cells were harvested by counting each cell line in quadruplicate and were resuspended in a known volume of lysis buffer [8 M urea, 1% CHAPS, and 20 mM Hepes (pH 8.0)]. The suspension was pulsed six times with a sonic dismembrator on ice and was rotated end over end for 1 hour at 4°C. DNA was pelleted, and cell lysate was prepared for MS analysis.

Cell lysates were prepared using the filter-aided sample preparation (FASP) method. Briefly, 50 to 200 μg of protein per sample, at a concentration of 1 to 10 μg/μl, was reduced with DTT (final concentration of 3 mM) at 57°C for 1 hour and loaded onto a MicroCon 30-kDa centrifugal filter unit pre-equilibrated with 200 μl of FASP buffer A [8 M urea and 0.1 M tris-HCl (pH 7.8)] (Millipore). Following three washes with FASP buffer A, lysates were alkylated on a filter with 50 mM iodoacetamide for 45 min in the dark. Filter-bound lysates were then washed three times each with FASP buffer A and FASP buffer B [100 mM ammonium bicarbonate (pH 7.8)] and were digested overnight at room temperature with trypsin (Promega) at a 1:100 ratio of enzyme to protein. Peptides were eluted twice with 0.5 M NaCl. Tryptic peptides were desalted using an UltraMicro Spin Column, C18, (Harvard Apparatus), and the desalted peptide mixture was concentrated in a SpeedVac concentrator.

Targeted MS assay development

Peptides used in this assay were selected on the basis of a series of experiments. First, we compiled data from the Global Proteome Machine Database (GPMDB) for each of the three proteins (*41*). GPMDB is a repository of the results of MS-based proteomics experiments. The data collected included the peptides and the charge states identified, their uniqueness to the protein, and the number of times that each was identified. The most often identified unique peptides and charge states of EED, EZH2, and SUZ12 were compared to the results of the recombinant analysis to generate a list of approximately five candidate peptides per protein.

Next, an equal molar trypsin-digested mixture of the three recombinant mouse PRC2 proteins (EED, EZH2, and SUZ12) was analyzed on a Q Exactive mass spectrometer (Thermo Fisher Scientific) using a data-dependent method. A list of identified proteotypic peptides was compiled. This list of peptides was used to generate a target list in the Skyline Software, which was used to build the targeted MS2 method. An aliquot of an mESC lysate was analyzed using this method. Raw files were uploaded to the Skyline Software. Candidate peptides were evaluated on the basis of the chromatographic peak shape, ionization efficiency, coverage of fragmentation, level of interference from other peptides within the isolation window, and the presence of product ions that differentiate the endogenous and heavy-labeled peptide. Two to three of the strongest candidate peptides were custom synthesized (New England Peptide) with an isotopically heavy C-terminal residue.

Targeted MS analysis

The peptides were spiked into an aliquot of the cell lysate at a level ranging from 100 amol to 5 fmol. The peptide mixture was loaded onto an Acclaim PepMap trap column in line with an EASY-Spray PepMap C18 analytical high-performance liquid chromatography (HPLC) column (inner diameter, 50 cm by 75 μm) with a 2-μm bead size using the auto sampler of an EASY-nLC 1000 HPLC (Thermo Fisher Scientific). The peptides were gradient eluted into a Q Exactive mass spectrometer (Thermo Fisher Scientific) using a 60-min gradient from 5 to 23% of solvent B (solvent A, 2% acetonitrile and 0.5% acetic acid; solvent B, 90% acetonitrile and 0.5% acetic acid), followed by 20 min from 23 to 45% of solvent B. Solvent B was taken to 100% in 10 min and held at 100% for 20 min. High-resolution full MS spectra were acquired with a resolution of 70,000, an automatic gain control (AGC) target of 1×10^6, a maximum ion time of 120 ms, and a scan range of 300 to 1500 mass/charge ratio (m/z). Following each full MS scan, targeted high-resolution high-energy collisional dissociation tandem MS (MS/MS) spectra were acquired on the basis of the inclusion list containing the m/z values of the unlabeled endogenous and stable isotope–labeled standard PRC2 peptides. All MS/MS spectra were collected using the following instrument parameters: resolution of 17,500, AGC target of 2×10^5, maximum ion time of 120 ms, one microscan, isolation window of 2.0 m/z, fixed first mass of 150 m/z, and normalized collision energy of 27. Peptides not behaving linearly in lysate were excluded from future quantitation.

Quantitative experiments were conducted in two ways: (i) five-point calibration curve (500 amol to 5 fmol) of standard peptides spiked into a constant amount of lysate or (ii) a single-point calibration of standard peptides spiked into a constant amount of lysate in triplicate in a concentration close or equal to the endogenous level.

Data analysis and validation

Raw files were uploaded to Skyline Software (64 bit) version 3.6.0.10162 for analysis. The top three or four product ions were used to quantify the light (endogenous) and stable isotope–labeled standard peptides (see data file S1). Total product ion area values were calculated for the light and heavy peptides.

When a calibration curve was generated, the total product ion area values for each of the stable isotope–labeled standard peptides were plotted, a linear trendline was fit to the data, and the line equation was used to calculate the femtomoles of endogenous peptide in the lysate. The average, SD, and the coefficient of variance across the triplicates are reported for all lysates.

To calculate the number of each PRC2 subunit (EZH2, EED and SUZ12) per cell, the average femtomoles is for each peptide quantified of that subunit were computed and converted to number of molecules using Avogadro's number and was divided by the number of cells analyzed to obtain molecules per cell. Total PRC2 per cell was calculated by taking the average of all subunits.

A few attempts have been made to infer the number of PRC2 molecules per nucleus using a variety of imaging and enzyme kinetic techniques. Reports vary from numbers as low as 6000 [acute lymphoblastic leukemia/myeloma; (*42*)] to ~40,000 [*Drosophila* neuroblast; (*43*)] and as high as 20,006,965 in a *Drosophila* salivary gland (*44*). While our methods provided slight variations on these numbers, they are well within the range and ordinal differences reported, adding validity to these various methods of PRC2 quantitation.

Histone extraction, MS, and analysis of histone modifications

Histone extraction, MS, and analysis of histone modifications were based on previously published methods (*45*, *46*). Quantifications for the histone modifications are presented in data file S2. All cell lines used for the analysis are noted in table S1.

ChIP-seq experiments

ChIP was performed as described previously (*40*). Briefly, H3.3K27M was induced by doxycycline (1 μg/ml) for 72 hours, cross-linked with 1% formaldehyde, and harvested following glycine treatment to quench the formaldehyde. Nuclei were extracted, sonicated using the Diagenode Bioruptor to produce chromatin fragments at an average size of 300 to 500 bp. Chromatin was then precleared with bovine serum albumin (BSA)–blocked magnetic Dynabeads. Each ChIP was performed with an internal spike-in standard corresponding to 1:200 of cross-linked, sonicated, and precleared *Drosophila* chromatin. The *Drosophila*-specific H2A.V antibody was also added at ~1:20 of the primary ChIP antibody. The immunoprecipitation was performed using antibodies to the appropriate protein (table S2) and 30 μl of BSA-blocked Dynabeads. Immunoprecipitated chromatin bound to the beads was then washed in radioimmunoprecipitation assay buffer. Chromatin was de–cross-linked, and proteins were removed by proteinase K. DNA libraries were constructed, barcoded as in (*17*), and subjected to SR50 sequencing on an Illumina HiSeq 2500 or Illumina NextSeq 500.

ChIP-seq data processing

Quality of sequencing was assessed with FastQC v0.11.4 (www.bioinformatics.babraham.ac.uk/projects/fastqc/). Reads having less than 80% of quality scores above 25 were removed with NGSQC-Toolkit v2.3.3 (*47*) using the command IlluQC.pl -se $file_path N A -l $percent -s $threshold -p $nb_cpu -o $out_path. Reads were aligned to the human hg19 reference genome from Illumina iGenomes University of California, Santa Cruz (UCSC) collection using bowtie v1.0.0 (*48*), allowing three mismatches and keeping uniquely aligned reads (bowtie -q -v 3 -p $nb_cpu -m 1 -k 1 --best --sam --seed 1 $bowtie_index_path "$file_path"). Sam (sequence alignment/map) outputs were converted to Bam (binary alignment/map) with SAMtools v1.0.6 (*49*) (samtools view -S -b $file_path -o $out_path/$file_name.bam) and were sorted with Picard tools v1.88 (http://broadinstitute.github.io/picard; java -jar SortSam.jar SO=coordinate I=$input_bam O=$output_bam). Data were further processed with Pasha v0.99.21 (*50*) with the following parameters: WIGvs = TRUE, incrArtefactThrEvery = 7,000,000, elongationSize = NA (not available). Fixed steps wiggle files were converted to bigwigs, with the

script wigToBigWig available on the UCSC Genome Browser website (http://hgdownload.soe.ucsc.edu/admin/exe/).

Spike-in normalization was achieved using *Drosophila melanogaster* DNA aligned to Illumina iGenomes dm3, as mentioned above (*51*). Endogenous and exogenous scaling factors were computed from the bam files [1/(number_mapped_reads/1,000,000)]. Endogenous scaling factors were applied to the data before input subtraction (without scaling). The reads per million reads normalization was then reversed before scaling with exogenous factors. The scripts used to perform spike-in scaling was integrated in the Bioconductor package ChIPSeqSpike (https://bioconductor.org/packages/3.7/bioc/html/ChIPSeqSpike.html).

Domain selection and peak calling

The different domains were identified in 293 T-REx cells at all time points with hiddenDomains v3.0 (*52*), with the command "hiddenDomains -g $chromInfo_file -b $bin_size -t $expBam -c $inputbam -o $outputFilePrefix." A window size of 50 or 100 kb was used (Figs. 2 and 3 and fig. S3 for example). To more precisely identify overlap between ChIPs within these domains, peaks were detected within the domain as noted in the main text and figure legends. Briefly, peaks were detected using SeqMonk v1.41 (www.bioinformatics.babraham.ac.uk/projects/seqmonk/), merging biological replicates using a 1×10^{-5} cutoff, filtered to identify only peaks contained within the domains, and transformed to the heatmap representation noted below (Figs. 2 and 3).

To retrieve the common K27me3 peaks by overlap in DIPG cells (Fig. 5), MACS2 v2.1.0 was used (macs2 callpeak -t $bam_file_vector -c $input_file_vector -n $experiment_name --outdir $output_folder_nomodel_broad -f $format -g $genome_size -s $tag_size --nomodel --extsize $elongation_size --keep-dup $artefact_threshold --broad --broad-cutoff 1×10^{-5}).

Metagene profiles and heatmaps

Metagene profiles and heatmap were largely generated with the Bioconductor package SeqPlots v1.8.1 (*53*) in command line. Mean, 95% confidence intervals, and SE are indicated on the profiles in the figures. Heatmaps for Figs. 2 and 3 and quantitative trend plots for Fig. 5 [1727 or all RefSeq (Reference Sequence) genes] were generated with deepTools v2.3.3 (*54*).

Western blot

Western blots were performed largely as in (*25*, *27*) with bis-tris–resolving gels and were transferred to 0.45-μm PVDF membranes. The antibodies used are indicated in the main text and table S2.

General quantitation and data analysis

Band intensity for Western blots and autoradiography experiments were quantitated after normalization using ImageJ. Where appropriate, simple a priori hypotheses were tested by analysis of variance (ANOVA), followed by Fisher's least significant difference. Experimental α was set to 0.05 for all experiments.

SUPPLEMENTARY MATERIALS

Supplementary material for this article is available at http://advances.sciencemag.org/cgi/content/full/4/10/eaau5935/DC1

Fig. S1. PRC2 quantitation across cell types.
Fig. S2. H3K36me2 is the predominant modification adjacent to K27M, and K27M is deposited primarily into active regions.
Fig. S3. The level of H3K27me3 at PRC2 common targeting domain is reduced in H3K27M cells.
Fig. S4. Cell line generation and characterization of PRC2 purified from H3.3K27M or H3.3K27WT cells.
Fig. S5. Alterations in histone modifications in H3K27M DIPG.
Fig. S6. Spreading of K36me2 in the K27M 293 T-REx cells.
Fig. S7. Select transcriptional changes associated with K36me2 in comparable K27M DIPG cell lines.
Table S1. Cell lines and tumor samples used in this study.
Table S2. Antibodies and relevant ChIP conditions used in this study.
Data file S1. Related to PRC2 quantitation.
Data file S2. Histone modification quantitation.

REFERENCES AND NOTES

1. P. B. Talbert, S. Henikoff, Histone variants on the move: Substrates for chromatin dynamics. *Nat. Rev. Mol. Cell Biol.* **18**, 115–126 (2017).
2. C. Jones, M. A. Karajannis, D. T. W. Jones, M. W. Kieran, M. Monje, S. J. Baker, O. J. Becher, Y.-J. Cho, N. Gupta, C. Hawkins, D. Hargrave, D. A. Haas-Kogan, N. Jabado, X.-N. Li, S. Mueller, T. Nicolaides, R. J. Packer, A. I. Persson, J. J. Phillips, E. F. Simonds, J. M. Stafford, Y. Tang, S. M. Pfister, W. A. Weiss, Pediatric high-grade glioma: Biologically and clinically in need of new thinking. *Neuro Oncol.* **19**, 153–161 (2016).
3. P. W. Lewis, M. M. Müller, M. S. Koletsky, F. Cordero, S. Lin, L. A. Banaszynski, B. A. Garcia, T. W. Muir, O. J. Becher, C. D. Allis, Inhibition of PRC2 activity by a gain-of-function H3 mutation found in pediatric glioblastoma. *Science* **340**, 857–861 (2013).
4. S. Bender, Y. Tang, A. M. Lindroth, V. Hovestadt, D. T. Jones, M. Kool, M. Zapatka, P. A. Northcott, D. Sturm, W. Wang, B. Radlwimmer, J. W. Højfeldt, N. Truffaux, D. Castel, S. Schubert, M. Ryzhova, H. Seker-Cin, J. Gronych, P. D. Johann, S. Stark, J. Meyer, T. Milde, M. Schuhmann, M. Ebinger, C. M. Monoranu, A. Ponnuswami, S. Chen, C. Jones, O. Witt, V. P. Collins, A. von Deimling, N. Jabado, S. Puget, J. Grill, K. Helin, A. Korshunov, P. Lichter, M. Monje, C. Plass, Y. J. Cho, S. M. Pfister, Reduced H3K27me3 and DNA hypomethylation are major drivers of gene expression in K27M mutant pediatric high-grade gliomas. *Cancer Cell* **24**, 660–672 (2013).
5. F. Mohammad, S. Weissmann, B. Leblanc, D. P. Pandey, J. W. Højfeldt, I. Comet, C. Zheng, J. V. Johansen, N. Rapin, B. T. Porse, A. Tvardovskiy, O. N. Jensen, N. G. Olaciregui, C. Lavarino, M. Suñol, C. de Torres, J. Mora, A. M. Carcaboso, K. Helin, EZH2 is a potential therapeutic target for H3K27M-mutant pediatric gliomas. *Nat. Med.* **23**, 483–492 (2017).
6. A. Piunti, R. Hashizume, M. A. Morgan, E. T. Bartom, C. M. Horbinski, S. A. Marshall, E. J. Rendleman, Q. Ma, Y. H. Takahashi, A. R. Woodfin, A. V. Misharin, N. A. Abshiru, R. R. Lulla, A. M. Saratsis, N. L. Kelleher, C. D. James, A. Shilatifard, Therapeutic targeting of polycomb and BET bromodomain proteins in diffuse intrinsic pontine gliomas. *Nat. Med.* **23**, 493–500 (2017).
7. K. Funato, T. Major, P. W. Lewis, C. D. Allis, V. Tabar, Use of human embryonic stem cells to model pediatric gliomas with H3.3K27M histone mutation. *Science* **346**, 1529–1533 (2014).
8. M. Pathania, N. De Jay, N. Maestro, A. S. Harutyunyan, J. Nitarska, P. Pahlavan, S. Henderson, L. G. Mikael, A. Richard-Londt, Y. Zhang, J. R. Costa, S. Hébert, S. Khazaei, N. S. Ibrahim, J. Herrero, A. Riccio, S. Albrecht, R. Ketteler, S. Brandner, C. L. Kleinman, N. Jabado, P. Salomoni, H3.3^{K27M} cooperates with Trp53 loss and PDGFRA gain in mouse embryonic neural progenitor cells to induce invasive high-grade gliomas. *Cancer Cell* **32**, 684–700.e9 (2017).
9. N. Justin, Y. Zhang, C. Tarricone, S. R. Martin, S. Chen, E. Underwood, V. De Marco, L. F. Haire, P. A. Walker, D. Reinberg, J. R. Wilson, S. J. Gamblin, Structural basis of oncogenic histone H3K27M inhibition of human polycomb repressive complex 2. *Nat. Commun.* **7**, 11316 (2016).
10. H.-M. Herz, M. Morgan, X. Gao, J. Jackson, R. Rickels, S. K. Swanson, L. Florens, M. P. Washburn, J. C. Eissenberg, A. Shilatifard, Histone H3 lysine-to-methionine mutants as a paradigm to study chromatin signaling. *Science* **345**, 1065–1070 (2014).
11. X. Wang, R. D. Paucek, A. R. Gooding, Z. Z. Brown, E. J. Ge, T. W. Muir, T. R. Cech, Molecular analysis of PRC2 recruitment to DNA in chromatin and its inhibition by RNA. *Nat. Struct. Mol. Biol.* **24**, 1028–1038 (2017).
12. K.-M. Chan, D. Fang, H. Gan, R. Hashizume, C. Yu, M. Schroeder, N. Gupta, S. Mueller, C. D. James, R. Jenkins, J. Sarkaria, Z. Zhang, The histone H3.3K27M mutation in pediatric glioma reprograms H3K27 methylation and gene expression. *Genes Dev.* **27**, 985–990 (2013).
13. Z. Z. Brown, M. M. Müller, S. U. Jain, C. D. Allis, P. W. Lewis, T. W. Muir, Strategy for "detoxification" of a cancer-derived histone mutant based on mapping its interaction with the methyltransferase PRC2. *J. Am. Chem. Soc.* **136**, 13498–13501 (2014).
14. P. Voigt, D. Reinberg, Putting a halt on PRC2 in pediatric glioblastoma. *Nat. Genet.* **45**, 587–589 (2013).
15. S. D. Sherrod, M. V. Myers, M. Li, J. S. Myers, K. L. Carpenter, B. Maclean, M. J. Maccoss, D. C. Liebler, A. J. Ham, Label-free quantitation of protein modifications by pseudo selected reaction monitoring with internal reference peptides. *J. Proteome Res.* **11**, 3467–3479 (2012).

16. C.-M. Shan, J. Wang, K. Xu, H. Chen, J.-X. Yue, S. Andrews, J. J. Moresco, J. R. Yates III, P. L. Nagy, L. Tong, S. Jia, A histone H3K9M mutation traps histone methyltransferase Clr4 to prevent heterochromatin spreading. *eLife* **5**, (2016).
17. V. Narendra, P. P. Rocha, D. An, R. Raviram, J. A. Skok, E. O. Mazzoni, D. Reinberg, CTCF establishes discrete functional chromatin domains at the *Hox* clusters during differentiation. *Science* **347**, 1017–1021 (2015).
18. D. Fang, H. Gan, L. Cheng, J.-H. Lee, H. Zhou, J. N. Sarkaria, D. J. Daniels, Z. Zhang, H3.3K27M mutant proteins reprogram epigenome by sequestering the PRC2 complex to poised enhancers. *eLife* **7**, e36696 (2018).
19. F. W. Schmitges, A. B. Prusty, M. Faty, A. Stützer, G. M. Lingaraju, J. Aiwazian, R. Sack, D. Hess, L. Li, S. Zhou, R. D. Bunker, U. Wirth, T. Bouwmeester, A. Bauer, N. Ly-Hartig, K. Zhao, H. Chan, J. Gu, H. Gut, W. Fischle, J. Müller, N. H. Thomä, Histone methylation by PRC2 is inhibited by active chromatin marks. *Mol. Cell* **42**, 330–341 (2011).
20. W. Yuan, M. Xu, C. Huang, N. Liu, S. Chen, B. Zhu, H3K36 methylation antagonizes PRC2-mediated H3K27 methylation. *J. Biol. Chem.* **286**, 7983–7989 (2011).
21. P. Voigt, G. LeRoy, W. J. Drury, B. M. Zee, J. Son, D. B. Beck, N. L. Young, B. A. Garcia, D. Reinberg, Asymmetrically modified nucleosomes. *Cell* **151**, 181–193 (2012).
22. W. Yuan, T. Wu, H. Fu, C. Dai, H. Wu, N. Liu, X. Li, M. Xu, Z. Zhang, T. Niu, Z. Han, J. Chai, X. J. Zhou, S. Gao, B. Zhu, Dense chromatin activates Polycomb repressive complex 2 to regulate H3 lysine 27 methylation. *Science* **337**, 971–975 (2012).
23. L. A. Banaszynski, D. Wen, S. Dewell, S. J. Whitcomb, M. Lin, N. Diaz, S. J. Elsässer, A. Chapgier, A. D. Goldberg, E. Canaani, S. Rafii, D. Zheng, C. D. Allis, Hira-dependent histone H3.3 deposition facilitates PRC2 recruitment at developmental loci in ES cells. *Cell* **155**, 107–120 (2013).
24. S. Kaneko, J. Son, R. Bonasio, S. S. Shen, D. Reinberg, Nascent RNA interaction keeps PRC2 activity poised and in check. *Genes Dev.* **28**, 1983–1988 (2014).
25. C. H. Lee, J. R. Yu, S. Kumar, Y. Jin, G. LeRoy, N. Bhanu, S. Kaneko, B. A. Garcia, A. D. Hamilton, D. Reinberg, Allosteric activation dictates PRC2 activity independent of its recruitment to chromatin. *Mol. Cell* **70**, 422–434.6 (2018).
26. H. Jayaram, D. Hoelper, S. U. Jain, N. Cantone, S. M. Lundgren, F. Poy, C. D. Allis, R. Cummings, S. Bellon, P. W. Lewis, S-adenosyl methionine is necessary for inhibition of the methyltransferase G9a by the lysine 9 to methionine mutation on histone H3. *Proc. Natl. Acad. Sci. U.S.A.* **113**, 6182–6187 (2016).
27. O. Oksuz, V. Narendra, C. H. Lee, N. Descostes, G. LeRoy, R. Raviram, L. Blumenberg, K. Karch, P. P. Rocha, B. A. Garcia, J. A. Skok, D. Reinberg, Capturing the onset of PRC2-mediated repressive domain formation. *Mol. Cell* **70**, 1149–1162.e5 (2018).
28. P. Pathak, P. Jha, S. Purkait, V. Sharma, V. Suri, M. C. Sharma, M. Faruq, A. Suri, C. Sarkar, Altered global histone-trimethylation code and H3F3A-ATRX mutation in pediatric GBM. *J. Neurooncol* **121**, 489–497 (2015).
29. S. Nagaraja, N. A. Vitanza, P. J. Woo, K. R. Taylor, F. Liu, L. Zhang, M. Li, W. Meng, A. Ponnuswami, W. Sun, J. Ma, E. Hulleman, T. Swigut, J. Wysocka, Y. Tang, M. Monje, Transcriptional dependencies in diffuse intrinsic pontine glioma. *Cancer Cell* **31**, 635–652 e636 (2017).
30. C. Lu, S. U. Jain, D. Hoelper, D. Bechet, R. C. Molden, L. Ran, D. Murphy, S. Venneti, M. Hameed, B. R. Pawel, J. S. Wunder, B. C. Dickson, S. M. Lundgren, K. S. Jani, N. De Jay, S. Papillon-Cavanagh, I. L. Andrulis, S. L. Sawyer, D. Grynspan, R. E. Turcotte, J. Nadaf, S. Fahiminiyah, T. W. Muir, J. Majewski, C. B. Thompson, P. Chi, B. A. Garcia, C. D. Allis, N. Jabado, P. W. Lewis, Histone H3K36 mutations promote sarcomagenesis through altered histone methylation landscape. *Science* **352**, 844–849 (2016).
31. R. Tatavosian, H. N. Duc, T. N. Huynh, D. Fang, B. Schmitt, X. Shi, Y. Deng, C. Phiel, T. Yao, Z. Zhang, H. Wang, X. Ren, Live-cell single-molecule dynamics of PcG proteins imposed by the DIPG H3.3K27M mutation. *Nat. Commun.* **9**, 2080 (2018).
32. C.-H. Lee, J. Granat, J.-R. Yu, G. LeRoy, J. Stafford, D. Reinberg, Automethylation of PRC2 fine-tunes its catalytic activity on chromatin. *bioRxivorg* 10.1101/349449 (2018).
33. X. Wang, Y. Long, R. D. Paucek, A. R. Gooding, T. Lee, T. R. Cech, Regulation of histone methylation by automethylation of PRC2. *bioRxivorg* 10.1101/343020 (2018).
34. L. Jiao, X. Liu, Structural basis of histone H3K27 trimethylation by an active polycomb repressive complex 2. *Science* **350**, aac4383 (2015).
35. R. Margueron, N. Justin, K. Ohno, M. L. Sharpe, J. Son, W. J. Drury III, P. Voigt, S. R. Martin, W. R. Taylor, V. De Marco, V. Pirrotta, D. Reinberg, S. J. Gamblin, Role of the polycomb protein EED in the propagation of repressive histone marks. *Nature* **461**, 762–767 (2009).
36. I. C. Taylor, M. Hütt-Cabezas, W. D. Brandt, M. Kambhampati, J. Nazarian, H. T. Chang, K. E. Warren, C. G. Eberhart, E. H. Raabe, Disrupting NOTCH slows diffuse intrinsic pontine glioma growth, enhances radiation sensitivity, and shows combinatorial efficacy with bromodomain inhibition. *J. Neuropathol. Exp. Neurol.* **74**, 778–790 (2015).
37. V. Caretti, A. C. Sewing, T. Lagerweij, P. Schellen, M. Bugiani, M. H. A. Jansen, D. G. van Vuurden, A. C. Navis, I. Horsman, W. P. Vandertop, D. P. Noske, P. Wesseling, G. J. L. Kaspers, J. Nazarian, H. Vogel, E. Hulleman, M. Monje, T. Wurdinger, Human pontine glioma cells can induce murine tumors. *Acta Neuropathol.* **127**, 897–909 (2014).
38. N. S. Bayin, J. D. Frenster, R. Sen, S. Si, A. S. Modrek, N. Galifianakis, I. Dolgalev, V. Ortenzi, I. Illa-Bochaca, A. Khahera, J. Serrano, L. Chiriboga, D. Zagzag, J. G. Golfinos, W. Doyle, A. Tsirigos, A. Heguy, M. Chesler, M. H. Barcellos-Hoff, M. Snuderl, D. G. Placantonakis, Notch signaling regulates metabolic heterogeneity in glioblastoma stem cells. *Oncotarget* **8**, 64932–64953 (2017).
39. A. S. Modrek, D. Golub, T. Khan, D. Bready, J. Prado, C. Bowman, J. Deng, G. Zhang, P. P. Rocha, R. Raviram, C. Lazaris, J. M. Stafford, G. LeRoy, M. Kader, J. Dhaliwal, N. S. Bayin, J. D. Frenster, J. Serrano, L. Chiriboga, R. Baitalmal, G. Nanjangud, A. S. Chi, J. G. Golfinos, J. Wang, M. A. Karajannis, R. A. Bonneau, D. Reinberg, A. Tsirigos, D. Zagzag, M. Snuderl, J. A. Skok, T. A. Neubert, D. G. Placantonakis, Low-grade astrocytoma mutations in IDH1, P53, and ATRX cooperate to block differentiation of human neural stem cells via repression of SOX2. *Cell Rep.* **21**, 1267–1280 (2017).
40. Z. Gao, J. Zhang, R. Bonasio, F. Strino, A. Sawai, F. Parisi, Y. Kluger, D. Reinberg, PCGF homologs, CBX proteins, and RYBP define functionally distinct PRC1 family complexes. *Mol. Cell* **45**, 344–356 (2012).
41. R. Craig, J. P. Cortens, R. C. Beavis, Open source system for analyzing, validating, and storing protein identification data. *J. Proteome Res.* **3**, 1234–1242 (2004).
42. Y. Zheng, S. M. M. Sweet, R. Popovic, E. Martinez-Garcia, J. D. Tipton, P. M. Thomas, J. D. Licht, N. L. Kelleher, Total kinetic analysis reveals how combinatorial methylation patterns are established on lysines 27 and 36 of histone H3. *Proc. Natl. Acad. Sci. U.S.A.* **109**, 13549–13554 (2012).
43. J. P. Fonseca, P. A. Steffen, S. Müller, J. Lu, A. Sawicka, C. Seiser, L. Ringrose, In vivo Polycomb kinetics and mitotic chromatin binding distinguish stem cells from differentiated cells. *Genes Dev.* **26**, 857–871 (2012).
44. G. Ficz, R. Heintzmann, D. J. Arndt-Jovin, Polycomb group protein complexes exchange rapidly in living *Drosophila*. *Development* **132**, 3963–3976 (2005).
45. K. R. Karch, S. Sidoli, B. A. Garcia, Identification and quantification of histone PTMs using high-resolution mass spectrometry. *Methods Enzymol.* **574**, 3–29 (2016).
46. G. Leroy, P. A. Dimaggio, E. Y. Chan, B. M. Zee, M. A. Blanco, B. Bryant, I. Z. Flaniken, S. Liu, Y. Kang, P. Trojer, B. A. Garcia, A quantitative atlas of histone modification signatures from human cancer cells. *Epigenetics Chromatin* **6**, 20 (2013).
47. R. K. Patel, M. Jain, NGS QC toolkit: A toolkit for quality control of next generation sequencing data. *PLOS ONE* **7**, e30619 (2012).
48. B. Langmead, C. Trapnell, M. Pop, S. L. Salzberg, Ultrafast and memory-efficient alignment of short DNA sequences to the human genome. *Genome Biol.* **10**, R25 (2009).
49. H. Li, B. Handsaker, A. Wysoker, T. Fennell, J. Ruan, N. Homer, G. Marth, G. Abecasis, R. Durbin; 1000 Genome Project Data Processing Subgroup, The sequence alignment/map format and SAMtools. *Bioinformatics* **25**, 2078–2079 (2009).
50. R. Fenouil, N. Descostes, L. Spinelli, F. Koch, M. A. Maqbool, T. Benoukraf, P. Cauchy, C. Innocenti, P. Ferrier, J.-C. Andrau, Pasha: A versatile R package for piling chromatin HTS data. *Bioinformatics* **32**, 2528–2530 (2016).
51. D. A. Orlando, M. W. Chen, V. E. Brown, S. Solanki, Y. J. Choi, E. R. Olson, C. C. Fritz, J. E. Bradner, M. G. Guenther, Quantitative ChIP-seq normalization reveals global modulation of the epigenome. *Cell Rep.* **9**, 1163–1170 (2014).
52. J. Starmer, T. Magnuson, Detecting broad domains and narrow peaks in ChIP-seq data with *hiddenDomains*. *BMC Bioinformatics* **17**, 144 (2016).
53. P. Stempor, J. Ahringer, SeqPlots—Interactive software for exploratory data analyses, pattern discovery and visualization in genomics. *Wellcome Open Res.* **1**, 14 (2016).
54. F. Ramirez, D. P. Ryan, B. Grüning, V. Bhardwaj, F. Kilpert, A. S. Richter, S. Heyne, F. Dündar, T. Manke, deepTools2: A next generation web server for deep-sequencing data analysis. *Nucleic Acids Res.* **44**, W160–W165 (2016).

Acknowledgments: We thank L. Vales and K.-J. Armache for critical guidance throughout the studies and critical reading of the manuscript. We thank P. Lee, S. Krishnan, E. Campos, A. Rojas, V. Narendra, and other past and current Reinberg laboratory members for discussion as the work was in progress. We are also grateful to D. Hernandez and N. Jahan for technical assistance and to M. Monje and E. Hulleman for providing DIPG/glioma cell lines that were integral to this work. **Funding:** The NYU Flow Cytometry Core, NYU Proteomics Laboratory, and NYU Genome Technology Center were partially supported by the NYU School of Medicine and the Laura and Isaac Perlmutter Cancer Center support grant, NCI (P30CA016087). The work was supported by grants to D.R. from NIH (R01CA199652), HHMI, and the Making Headway Foundation (189290). A grant from the Hyundai Hope on Wheels Foundation to M.S. and D.R. partially supported this work. Molecular profiling of human samples was in part supported by grants from the Friedberg Charitable Foundation, the Rachel Molly Markoff Foundation, and the Sohn Conference Foundation to M.S. This work was partially supported by a junior fellow award from the Simons Foundation and by an NIH grant (K99AA024837) to J.M.S. J-R.Y. was supported by the American Cancer Society (PF-17-035-01). P.V. was supported by the Empire State Training Program in Stem Cell Research (NYSTEM; contract no. C026880).
Author contributions: J.M.S., C.-H.L., P.V., and D.R. conceptualized and designed the study. J.M.S., C.-H.L., P.V., J.-R.Y., G.L., O.O., and F.S. conducted the experiments. N.D. and R.S.-M. performed the bioinformatics analyses. J.R.C. and B.U. performed MS analyses. A.S.M., N.S.B., D.G.P., M.A.K., and M.S. provided guidance on brain tumor models and provided cell lines/banked tumors. J.M.S., C.-H.L., R.S.-M., N.D., and D.R. wrote the manuscript. **Competing**

interests: D.R. is a co-founder of Constellation Pharmaceuticals and Fulcrum Therapeutics. All other authors declare that they have no competing interests. **Data and materials availability:** Data and relevant computations for the proteomics work are presented in data files S1 and S2. The accession number for the ChIP-seq and RNA-seq results reported in this paper is Gene Expression Omnibus (GEO) no. GSE118954. We are appreciative of the DIPG/glioma cell lines provided under material transfer agreement by M. Monje and E. Hulleman and therefore will route any request for those reagents to them upon inquiry. All data needed to evaluate the conclusions in the paper are present in the paper and/or the Supplementary Materials. Additional data related to this paper may be requested from the authors.

Submitted 26 June 2018
Accepted 27 September 2018
Published 31 October 2018
10.1126/sciadv.aau5935

Citation: J. M. Stafford, C.-H. Lee, P. Voigt, N. Descostes, R. Saldaña-Meyer, J.-R. Yu, G. Leroy, O. Oksuz, J. R. Chapman, F. Suarez, A. S. Modrek, N. S. Bayin, D. G. Placantonakis, M. A. Karajannis, M. Snuderl, B. Ueberheide, D. Reinberg, Multiple modes of PRC2 inhibition elicit global chromatin alterations in H3K27M pediatric glioma. *Sci. Adv.* **4**, eaau5935 (2018).